EPJ Web of Conferences **71**, 00124 (2014)
DOI: 10.1051/epjconf/20147100124

Measurements of properties of the Higgs-like boson in the $H \to ZZ^{(*)} \to 4\ell$ decay channel using the ATLAS detector

Stahlman, JM,[1,a] on behalf of the ATLAS Collaboration.

[1] *University of Pennsylvania*

Abstract. This article presents results on measurements of the signal strength, mass, and spin of the recently discovered Higgs-like boson in the $H \to ZZ^{(*)} \to 4\ell$ decay channel using the ATLAS detector. The results are based on the combined dataset of the 2011 and 2012 LHC runs consisting of 4.6 fb^{-1} of $\sqrt{s} = 7$ TeV and 20.7 fb^{-1} of $\sqrt{s} = 8$ TeV proton-proton collision data. An excess of events is observed corresponding to $m_H = 124.3$ GeV with a p_0 value of 2.7×10^{-11} (6.6 standard deviations). The fit at this mass point yields a signal strength relative to the SM of $1.7^{+0.5}_{-0.4}$ with $m_H = 124.3^{+0.6}_{-0.5}$ (stat)$^{+0.5}_{-0.3}$ (syst) GeV. Tests of various spin-parity hypotheses are also presented, with the 0^- and 1^+ hypotheses being excluded versus the 0^+ hypothesis at >97% confidence level.

1 Introduction

The recent observation of a Higgs-like boson [1, 2] was a major success for the ATLAS and CMS experiments at the LHC. Determining whether this newly-discovered particle is compatible with the Standard Model (SM) predictions for the Higgs boson or not is now of utmost importance. The $H \to ZZ^{(*)} \to 4\ell$ ($\ell = e, \mu$) decay channel is important in these measurements due to the small well-constrained backgrounds and full reconstruction of all decay products of the Higgs boson. This article presents an overview of measurements [3] of the signal strength (inclusive and separated into production modes) and mass as well as hypothesis tests of the spin-parity state of the new boson in the $H \to ZZ^{(*)} \to 4\ell$ channel. Section 2 describes the experimental setup of the ATLAS detector. Section 3 describes the simulation used. Section 4 discusses the object and event selection and the backgrounds are explained in Section 5. Section 6 will detail the associated systematics. In Section 7, the results are presented and Section 8 contains concluding remarks.

2 Detector

The ATLAS detector [4] is a multipurpose symmetric cylindrical detector and consists of three main components, the Inner Detector (ID), the calorimeters, and the Muon Spectrometer (MS). The ID provides tracking of charged particles within $|\eta|$[1] of 2.5 with transverse momentum $p_T > 0.5$ GeV. It consists of pixel and silicon strip detectors surrounded by a gaseous straw tube tracker. The ID is surrounded by a thin superconducting solenoid which provides a 2 T magnetic field. Moving outwards,

[a] e-mail: stahlman@sas.upenn.edu

liquid-argon (LAr) and steel-scintillator tile calorimeters provide electromagnetic and hadronic energy measurements within $|\eta| < 4.5$. Outside of the calorimeters, the MS provides muon tracking up to $|\eta|$ of 2.7 in a 1.4 Tesla magnetic field created by a set of superconducting air core toroidal magnets.

3 Simulation

The $H \rightarrow 4\ell$ signal is modelled using the Powheg Monte Carlo (MC) event generator [5], which calculates separately the gluon fusion (ggF) and vector-boson fusion (VBF) production mechanisms with matrix elements up to next-to-leading order (NLO). The description of the Higgs boson transverse momentum spectrum in the ggF process follows the calculation of Ref. [6], which includes QCD corrections up to NLO and QCD soft-gluon re-summations up to next-to-next-to-leading logarithm (NNLL). Powheg is interfaced to Pythia [7] for showering and hadronization, which in turn is interfaced to Photos [8, 9] for quantum electrodynamics (QED) radiative corrections in the final state. Pythia is used to simulate the production of a Higgs boson in association with a W or a Z boson (VH) and with a $t\bar{t}$ pair ($t\bar{t}H$).

The Higgs boson production cross sections and decay branching ratios, as well as their uncertainties, are taken from Refs. [10, 11]. The Higgs boson decay branching ratios [12] to the different four-lepton final states are provided by Prophecy4f [13, 14], which includes the complete NLO QCD+EW corrections and interference effects between identical final-state fermions.

The $ZZ^{(*)}$ continuum background is modelled using Powheg [15] for quark-antiquark annihilation and `gg2ZZ` [16] for gluon-gluon contributions, normalised to the MCFM prediction [17]. The $ZZ^{(*)}qq'$ continuum background is modelled using Sherpa [18]. Tauola [19, 20] is used for the simulation of τ lepton decays which come from both signal and background Z decays.

The Z+jets production is modelled using Alpgen [21] and is divided into two sources: Z+light jets, which includes $Zc\bar{c}$ in the massless c-quark approximation and $Zb\bar{b}$ with $b\bar{b}$ from parton showers, and $Zb\bar{b}$ using matrix element calculations that take into account the b-quark mass. The $t\bar{t}$ background is modelled using MC@NLO [22] and is normalised to the approximate NNLO cross section calculated using Hathor [23]. Both Alpgen and MC@NLO are interfaced to Herwig [24] for parton shower hadronization and to Jimmy [25] for the underlying event simulation.

Generated events are fully simulated using the ATLAS detector simulation [26] within the Geant4 framework [27]. Additional pp interactions in the same and nearby bunch crossings (pile-up) are included in the simulation. The MC samples are re-weighted to reproduce the observed distribution of the mean number of interactions per bunch crossing in the data.

4 Event Selection

The event selection is driven by the identification of the four isolated electrons and/or muons in the final state from the Higgs decay. The selection has been optimized to maximize signal efficiency while maintaining reasonable background levels.

[1] The nominal interaction point is defined as the origin of the coordinate system, while the anti-clockwise beam direction defines the z-axis and the x–y plane is transverse to the beam direction. The positive x-axis is defined as pointing from the interaction point to the center of the LHC ring and the positive y-axis is defined as pointing upwards. The azimuthal angle ϕ is measured around the beam axis and the polar angle θ is the angle from the beam axis. The pseudorapidity is defined as $\eta = -\ln(\tan(\theta/2))$.

4.1 Lepton Selection

Electron candidates are reconstructed from well-measured ID tracks which are matched to clusters of electromagnetic energy in the LAr calorimeters [28]. Tracks associated with electron candidates are re-fit using a Gaussian-Sum Filter technique [29] which takes into account energy loss caused by the emission of bremsstrahlung. Electrons are required to have $p_T > 7$ GeV and $|\eta| < 2.47$.

A variety of backgrounds, including hadronic jets, pions, and photon conversions, can be misidentified as electrons. To reduce these backgrounds, cuts are applied on the shower shapes and track matching of the associated clusters of energy in the electromagnetic and hadronic calorimeters. Furthermore, a hit requirement in the first layer of the pixel tracker is required in order to reduce backgrounds from photon conversions. Reconstruction and identification efficiencies of >90% are achieved over the entire E_T range.

Muon candidates are reconstructed by combining well-reconstructed ID tracks with MS tracks [30]. Furthermore, additional muon candidates are allowed in regions of the detector where standard muon efficiency is low: ID track only muons within $|\eta| < 0.1$ and MS track only muons in the forward regions ($2.5 < |\eta| < 2.7$). At most one of these ID or MS only muons is allowed to be selected per quadruplet. Reconstruction efficiencies of > 98% are achieved over almost the entire detector volume. Muons are required to have $p_T > 6$ GeV and $|\eta| < 2.7$.

4.2 Quadruplet Selection

The reconstructed leptons in each event are grouped into quadruplets consisting of two same flavor opposite sign pairs. The quadruplets are required to contain leptons which fired the trigger and the leading three leptons must have p_T greater than 20, 15, and 10 GeV. The invariant mass of the lepton pair closest to the PDG Z mass (the leading pair) is designated as m_{12} and the invariant mass of the other pair is m_{34}. The invariant mass of the four leptons in the quadruplet, $m_{4\ell}$, is the primary discriminating variable. The quadruplet is also categorized according to the flavor of the leptons: 4μ, $2e2\mu$, or $4e$.

If more than one quadruplet is found in an event, one quadruplet is chosen by first selecting all quadruplets with m_{12} closest to the PDG Z mass. From those, the quadruplet with m_{34} closest to the PDG Z mass is chosen. The following requirements are then applied to the chosen quadruplet in order to further reduce backgrounds:

- $50 < m_{12} < 106$ GeV
- $m_{cut} < m_{34} < 115$ GeV
- $m_{\ell\ell} > 5$ GeV for alternative same-flavor opposite charge pairings (J/Ψ veto)
- $\Delta R(\ell, \ell') > 0.10$ (0.20) for all same (different) flavor leptons
- Isolation requirements using both track and calorimeter information
- Impact parameter significance requirements

m_{cut} varies with $m_{4\ell}$: the value of m_{cut} is 12 GeV for $m_{4\ell}$ <140 GeV, rises linearly to 50 GeV with $m_{4\ell}$ in the interval 140 GeV to 190 GeV and remains at 50 GeV for $m_{4\ell}$ >190 GeV.

With this selection, the total signal efficiency for the 8 (7) TeV data is estimated to be 39/26/19% (39/21/15%) in the $4\mu/2e2\mu/4e$ channels.

4.3 Event Categorisation

Separation of the candidate events into ggF-like, VBF-like, and VH-like categories is done after the event selection in order to measure cross sections of the various Higgs production modes. The categorisation requires the presence of additional objects, such as leptons and/or jets, in order to discriminate between the various production modes. These additional objects originate from decays of other particles produced in association with the Higgs boson.

Jets are reconstructed from topological clusters in the calorimeter using an anti-kT algorithm [31] with distance parameter R = 0.4. Jets are required to be within the acceptance of the calorimeter ($|\eta| < 4.5$) and to have $p_T > 25$ (30) GeV in the range $|\eta| < |2.5|$ ($2.5 < |\eta| < 4.5$). Furthermore, if a jet is within the ID acceptance ($|\eta| < 2.47$), 50% or more of the scalar sum p_T of the tracks associated with the jet must originate from the primary vertex in order to reduce jets from background due to pile-up.

VBF-like events are required to have at least two high p_T jets. The two highest p_T jets are required to be separated by at least 3 units of pseudorapidity and have an invariant mass greater than 350 GeV. Events not satisfying the VBF-like criteria are then considered for the VH category. Events are classified as VH-like if they contain a muon or electron with $p_T > 8$ GeV in addition to the 4 previously selected leptons. Events which are not categorized as VBF-like or VH-like are categorized as ggF-like.

5 Background Estimation

The backgrounds to this analysis are grouped into two categories, irreducible and reducible. Irreducible backgrounds produce the same final state particles (4 isolated leptons) as the signal and as such are difficult to reduce without significant decrease in signal efficiency. The reducible backgrounds are present due to processes in which other particles (jets, photons, etc.) are mis-reconstructed as leptons.

5.1 Irreducible Backgrounds

The irreducible background consists primarily of SM $ZZ^{(*)}$ production. The normalization and shape in $m_{4\ell}$ for this background are taken entirely from the simulation. The contribution from the $ZZ^{(*)}$ background is constrained in the $m_{4\ell}$ fit by regions in $m_{4\ell}$ which are far away from the narrow peak of the signal. In particular, there are two features which are dominated by $ZZ^{(*)}$ production: the single resonant Z peak located at the Z mass and the resonant $ZZ^{(*)}$ production at $m_{4\ell}$ of roughly twice the Z mass, as seen in Figure 1. Excellent agreement between the data and background prediction is observed in both of these regions.

5.2 Reducible Backgrounds

The reducible background consists primarily of Z+jets and $t\bar{t}$ production where 2 or more quarks either decay semi-leptonically producing real leptons or the hadronisation of the quarks is mis-reconstructed as leptons. Because there are large uncertainties associated with the modeling of jets faking leptons, all reducible background yields are estimated using data-driven techniques.

The composition of the reducible background depends strongly on the flavor of the subleading leptons. Therefore, the background estimation method differs for each flavor of subleading leptons. The general strategy in these estimates is to define background-enriched data control regions by relaxing cuts on the subleading leptons. Efficiencies for these relaxed cuts are estimated in auxiliary measurements. The signal region yield is then extrapolated from the control region yields using these efficiencies.

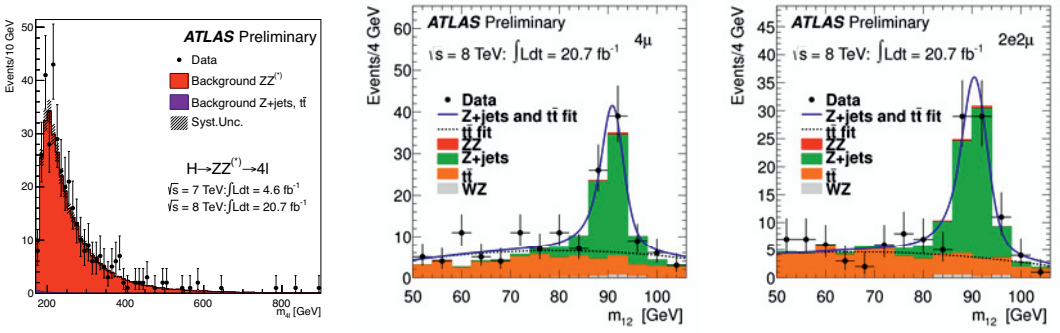

(a) (b) (c)

Figure 1: (a) The contribution from SM ZZ production is constrained by the ZZ resonance at twice the Z mass. (b) Fit of m_{12} distributions for $\ell\ell + \mu\mu$ control regions in the (b) 4μ channel and (c) $2e2\mu$ channel [3].

5.2.1 $\ell\ell + \mu\mu$ background

A control region for the $\ell\ell + \mu\mu$ background is defined by removing the isolation requirement on the subleading muons and requiring at least one subleading muon to fail the impact parameter significance requirement. This selection enhances the $t\bar{t}$ and heavy flavor decays of Z+jets while suppressing the $ZZ^{(*)}$ contribution. The yields in the control region for these backgrounds are extracted by fitting the m_{12} distribution as seen in Figure 1.

5.2.2 $\ell\ell + ee$ background

Electron candidates will contain contributions from heavy flavor semi-leptonic decays, photon conversions, and light flavor jets mis-reconstructed as electrons. A control region for the $\ell\ell + ee$ background is defined by relaxing the electron identification criteria on the subleading electrons. The efficiencies to extrapolate from the relaxed identification to the standard identification are measured in the simulation and cross-checked in data for each of the background processes. Furthermore, the subleading electrons of events in the control region are categorized as electron-like or fake-like using tracking and calorimeter variables. This categorization is used to control for the composition of the control region when extrapolating the control region yields to the signal region yields. This procedure is cross-checked with two other estimation methods and good agreement between the methods is observed.

6 Systematics

Systematic uncertainties due to lepton reconstruction and identification uncertainties as well as energy or momentum scale and resolution uncertainties are estimated by studying samples of W, Z, and J/Ψ decays. Table 1 summarizes the systematic uncertainties associated with the signal yield. Mass scale systematics are estimated to be 0.2%/0.4%/0.1%/0.2% for the 4μ/4e/2μ2e/2e2μ channel.

Individual Channel Systematics				
	4 μ	2e2μ	4e	2μ2e
Electron Reco and ID	-	2.4%	9.4%	8.7%
Muon Reco and ID	0.8%	0.4%	-	0.4%

Inclusive Systematics	
Luminosity	1.8% (3.6%) 2011 (2012)
PDF +α_s	8%
QCD scale	+7% -8%

Table 1: Signal yield systematic uncertainties [3].

$\sqrt{s}$ = 8 TeV and $\sqrt{s}$ = 7 TeV							
	total signal full mass range	signal	$ZZ^{(*)}$	Z + jets, $t\bar{t}$	S/B	expected	observed
4μ	6.8 ± 0.8	6.3 ± 0.8	2.8 ± 0.1	0.55 ± 0.15	1.9	9.6 ± 1.0	13
2μ2e	3.4 ± 0.5	3.0 ± 0.4	1.4 ± 0.1	1.56 ± 0.33	1.0	6.0 ± 0.8	5
2e2μ	4.7 ± 0.6	4.0 ± 0.5	2.1 ± 0.1	0.55 ± 0.17	1.5	6.6 ± 0.8	8
4e	3.3 ± 0.5	2.6 ± 0.4	1.2 ± 0.1	1.11 ± 0.28	1.1	4.9 ± 0.8	6
total	18.2 ± 2.4	15.9 ± 2.1	7.4 ± 0.4	3.74 ± 0.93	1.4	27.1 ± 3.4	32

Table 2: The number of expected signal events for the m_H=125 GeV hypothesis and background events together with the numbers of observed events, in a window of ±5GeV around 125 GeV [3].

7 Results

The $m_{4\ell}$ distribution of candidate events is seen in Figure 2. A clear peak over the predicted background is observed at $m_{4\ell} \sim 125$ GeV. The full results of the analysis are presented as follows: Section 7.1 describes the mass and signal strength measurements, Section 7.2 describes the spin-parity hypothesis testing and Section 7.3 describes the results of the event categorization.

7.1 Signal Strength and Mass

In Table 2, the predicted and observed yields for the combined 2011 and 2012 dataset in a mass window of ± 5 GeV around $m_{4\ell} = 125$ GeV are presented. An unbinned maximum-likelihood fit of signal and background models to the observed $m_{4\ell}$ distribution was performed and the best fit point corresponds to $m_H = 124.3$ GeV with a signal strength (the ratio of observed events to predicted events) $\mu = 1.7^{+0.5}_{-0.4}$.

The significance of an excess is given by the probability p_0, that a background-only experiment is more signal-like in terms of the test statistic than the observed data. The local p_0 value is shown as a function of m_H in Figure 2. The minimum p_0 observed for the dataset is 2.7×10^{-11} (6.6 standard deviations, 4.4 expected) at $m_H = 124.3$ GeV, which surpasses the 5σ requirement for discovery.

The signal model in the maximum-likelihood fit is derived entirely from simulation of the SM Higgs boson and is described using smooth, non-parametric, unbinned estimates of the probability density function. The $m_{4\ell}$ shape, normalization and systematic uncertainties are parametrized as a function of m_H allowing for a maximum-likelihood fit to determine the best fit value of m_H. Figure 2

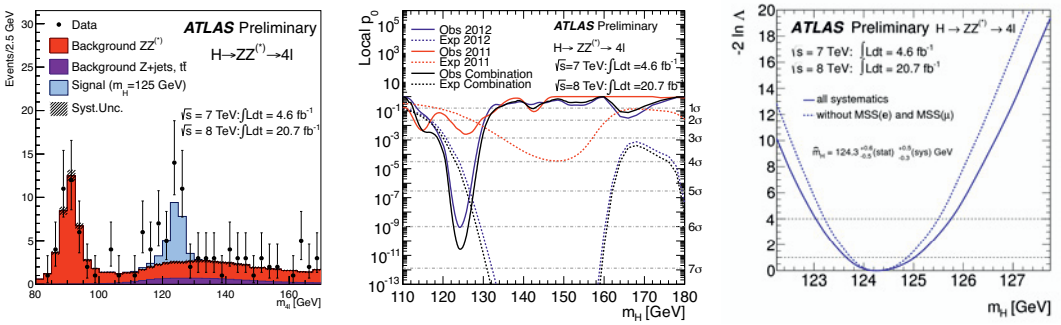

(a) (b) (c)

Figure 2: (a) $m_{4\ell}$ distribution for event candidates in the signal region with $\mu = 1$ and $M_H = 125$ GeV prediction overlaid. (b) Local p_0 value and (c) profile likelihood as a function of M_H [3].

shows the profile likelihood as a function of m_H. The best fit value is $m_H = 124.3^{+0.6}_{-0.5}(\text{stat})^{+0.5}_{-0.3}(\text{syst})$ GeV. The systematic uncertainty is dominated by the energy and momentum scale systematics.

7.2 Spin Parity

For $X \to ZZ^{(*)} \to 4\ell$ decays, the observables sensitive to the spin and parity of X are m_{12}, m_{34}, a production angle, θ^*, and four decay angles, ϕ_1, ϕ, θ_1 and θ_2 [3]. In this analysis, six hypotheses for spin/parity states are tested: $J^P = 0^\pm, 1^\pm, 2^\pm$. The spin-2 states are modeled as a graviton-like tensor with minimal couplings, equivalent to a Kaluza Klein graviton (2^+_m), and a pseudo-tensor (2^-). The spin-2 states can be produced via gluon fusion and $q\bar{q}$ annihiliation with different final state angular distributions. Because the relative ratio of these production methods is not determined by the theory, different mixtures were tested in steps of 25% for the 2^+_m state.

The event selection for the spin parity measurements is the same as in Section 4. The events in the mass window were split into two categories of low and high signal over background: low (115-121 GeV and 127-130 GeV) and high (121-127 GeV). Two different analyses were performed to distinguish between the various spin parity states. The first uses a boosted decision tree (BDT) to produce a discriminant based on the spin parity variables for each pairwise hypothesis tests (with the exception of θ^* and ϕ_1 in the 0^+ vs. 0^- test). The second uses differential decay rates of the discriminating variables from theory (corrected for detector acceptance and efficiency) in order to construct a matrix element based likelihood ratio (MELA) [32].

The statistical test for a pair of spin-parity hypotheses, H_0 and H_1, uses the probability model:

$$\mathcal{P}^{ij} = \mu^{\text{sig}} f_i^{\text{sig}} N_{\text{sig}} \left[(1-\varepsilon) \cdot \text{PDF}^{ij}_{H_0} + \varepsilon \cdot \text{PDF}^{ij}_{H_1} \right] + \sum_{\text{bkg}_k} f_i^{\text{bkg}_k} N_{\text{bkg}_k} \text{PDF}^{\text{ij}}_{\text{bkg}_k},$$

where μ^{sig} is the signal strength, N_{sig} is the number of expected SM signal events in the full mass region ($115\,\text{GeV} < m_{4\ell} < 130\,\text{GeV}$), f_i^{sig} is the signal fraction in the i^{th} S/B mass region (low and high), and $(1-\varepsilon)$ is the fraction of the H_0 signal hypothesis represented by the $\text{PDF}^{ij}_{H_0}$ for the j^{th} J^P discriminant. Similarly, $f_i^{\text{bkg}_k}$, N_{bkg_k} and $\text{PDF}^{\text{ij}}_{\text{bkg}_k}$ are the region fraction, total background and PDF for the k^{th} background, respectively.

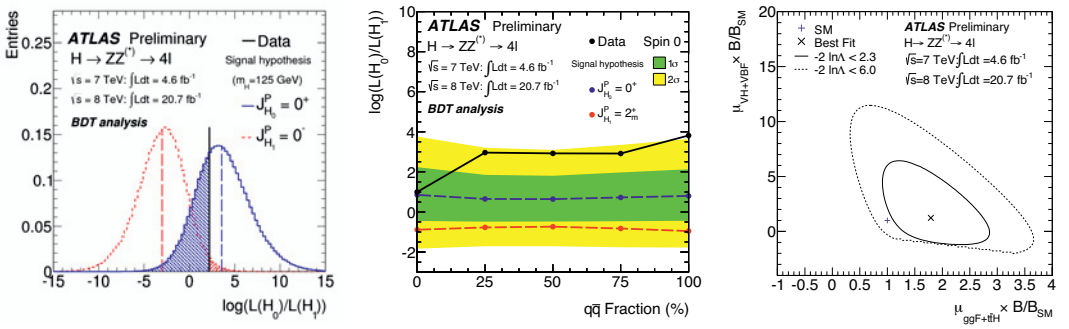

(a) (b) (c)

Figure 3: (a) Test statistic for discriminating 0^- versus the 0^+ hypothesis using the BDT approach and (b) Test statistic for discriminating different mixtures of ggF and $q\bar{q}$ production of 2^+_m hypotheses versus the 0^+ hypothesis using the BDT approach. The observed value is in black and the expected 1 (2) σ bands are given in green (yellow) assuming the SM hypothesis 0^+ and (c) likelihood contours in the $(\mu_{ggF+t\bar{t}H}, \mu_{VBF+VH})$ plane including the branching ratio factor B/B_{SM} [3].

The test statistic used is the log-likelihood ratio of fitted likelihoods $\log[L(H_1)/L(H_0)]$, where the parameter ε is 0 for the assumed H_0 hypothesis and 1 for the tested H_1 hypothesis. The probability model is fitted to the data to obtain a maximum likelihood estimate for the nuisance parameters. Then a series of pseudo-experiments is generated to construct the sampling distributions for the two hypotheses.

An example plot of the test statistic used for testing the 0^- versus the 0^+ hypotheses is seen in Figure 3a. Table 3 gives the results of all tests when the 0^+ hypothesis is assumed. Both approaches show similar sensitivity, with the expected sensitivity to discriminate the 0^-, 1^+, 1^-, and 2^- above the 2.5σ level. The 0^-, 1^+, and 1^- hypotheses are excluded at >95 % CL_S confidence levels in favor of the 0^+ hypothesis in both approaches. Furthermore, the results for the ggF/$q\bar{q}$ mixtures are given in Figure 3b.

		BDT analysis				J^PMELA analysis			
		tested J^P for an assumed 0^+		tested 0^+ for an assumed J^P	CL_S	tested J^P for an assumed 0^+		tested 0^+ for an assumed J^P	CL_S
		expected	observed	observed*		expected	observed	observed*	
0^-	p_0	0.0037	0.015	0.31	0.022	0.0011	0.0022	0.40	0.004
1^+	p_0	0.0016	0.001	0.55	0.002	0.0031	0.0028	0.51	0.006
1^-	p_0	0.0038	0.051	0.15	0.060	0.0010	0.027	0.11	0.031
2^+_m	p_0	0.092	0.079	0.53	0.168	0.064	0.11	0.38	0.182
2^-	p_0	0.0053	0.25	0.034	0.258	0.0032	0.11	0.08	0.116

Table 3: For an assumed 0^+ hypothesis H_0, the expected and observed p_0-values of the different tested spin and parity hypotheses H_1 for the BDT and J^P MELA analyses. Also given is the observed p_0-value where 0^+ is the test hypothesis and the other spins states are the assumed hypothesis (observed*) [3].

7.3 Production Modes

The predicted and observed yields in the various categories are presented in Table 4. One candidate VBF event is observed in the mass window of 120-130 GeV around the observed signal with $m_{4\ell}$ = 123.5 GeV. In this mass window, 0.71± 0.10 signal events are expected from a SM Higgs boson and the signal-to-background ratio is estimated to be approximately 5. Away from the signal region (above 160 GeV), the yields of the VBF and VH candidates are consistent with the predicted background.

The global strength measurement is modified to allow signal strength measurement for specific production modes using this categorisation. In this analysis, the production mechanisms are separated into a "fermionic" group consisting of ggF and $t\bar{t}H$ and a "bosonic" group consisting of the VBF and VH modes. In Figure 3c the best fit values $\mu_{\mathrm{ggF}+t\bar{t}H} \times B/B_{\mathrm{SM}}$ and $\mu_{\mathrm{VBF+VH}} \times B/B_{\mathrm{SM}}$ are presented. The factor B/B_{SM}, the scale factor of the branching ratio with respect to the SM value, is included because a single channel analysis cannot differentiate production and decay couplings. The measured values for $\mu_{\mathrm{ggF}+t\bar{t}H} \times B/B_{\mathrm{SM}}$ and $\mu_{\mathrm{VBF+VH}} \times B/B_{\mathrm{SM}}$ are $1.8^{+0.8}_{-0.5}$ and $1.2^{+3.8}_{-1.4}$, respectively.

category	$gg \to H, q\bar{q}/gg \to t\bar{t}H$	$qq' \to Hqq'$	$q\bar{q} \to W/ZH$	$ZZ^{(*)}$	observed
$\sqrt{s}$ = 8 TeV and $\sqrt{s}$ = 7 TeV					
ggF-like	15.7	0.93	0.76	377.9	450
VBF-like	0.31	0.49	0.01	4.02	8
VH-like	0.07	-	0.17	0.94	1

Table 4: The expected numbers of events in each category (ggF-like, VBF-like, VH-like), after all analysis criteria are applied, for each signal production mechanism (ggF/$t\bar{t}H$, VBF, VH) at m_H =125 GeV and the $ZZ^{(*)}$ background and the total number of events observed in each category in the full dataset. The requirement $m_{4\ell} > 100$ GeV is applied [3].

8 Conclusions

Results of property measurements of the newly observed Higgs-like boson have been presented for the $H \to 4\ell$ channel using the full 2011+2012 LHC datasets as recorded by the ATLAS detector. An excess of events over the background is observed with the minimum p_0 of 2.7×10^{-11} (6.6 standard deviations), surpassing the 5σ requirement for discovery. The best fitted mass is $m_H = 124.3^{+0.6}_{-0.5}\,(\mathrm{stat})^{+0.5}_{-0.3}\,(\mathrm{syst})$ GeV and the signal strength (the ratio of the observed cross section to the expected SM cross section) of the Higgs-like boson at this mass is found to be $1.7^{+0.5}_{-0.4}$.

Hypothesis tests comparing the SM 0^+ J^P hypothesis with 0^-, 1^+, 1^-, 2^+_m and 2^- have been presented. The 0^+ hypothesis has also been compared to the 2^+_m hypothesis for varying fractions of ggF and $q\bar{q}$ production. The expected separation is found to be independent of the production fractions. The Higgs-like boson is found to be compatible with the SM expectation of 0^+ when compared pairwise with 0^-, 1^+, 1^-, 2^+, and 2^-. The 0^- and 1^+ states are excluded at the 97.8% confidence level or higher using $\mathrm{CL_S}$ in favour of 0^+.

Finally, the $H \to 4\ell$ candidate events have been categorised, allowing the study of Higgs boson couplings via the separation of ggF/$t\bar{t}H$ and VBF/VH production. A VBF-like candidate has been observed at 123.5 GeV, where approximately 0.4 VBF events and 0.3 ggF events are expected with S/B ~ 5.

For all measurements, no significant deviations from the SM predictions have been observed. Because the uncertainties in these measurements are currently statistically dominated, this analysis will benefit greatly from the addition of the forthcoming LHC data at higher energies and larger integrated luminosities.

References

[1] ATLAS Collaboration, Phys. Lett. **B716**, 1 (2012), 1207.7214
[2] CMS Collaboration, Phys. Lett. **B716**, 30 (2012), 1207.7235
[3] ATLAS Collaboration, ATLAS-CONF-2013-013 (2013)
[4] ATLAS Collaboration, JINST **3**, S08003 (2008)
[5] S. Alioli, P. Nason, C. Oleari, E. Re, JHEP **04**, 002 (2009), 0812.0578
[6] D. de Florian, G. Ferrera, M. Grazzini, D. Tommasini, JHEP **11**, 064 (2011), 1109.2109
[7] T. Sjostrand, S. Mrenna, P.Z. Skands, JHEP **05**, 026 (2006), hep-ph/0603175
[8] P. Golonka, Z. Was, Eur. Phys. J. **C 45**, 97 (2006), hep-ph/0506026
[9] N. Davidson, T. Przedzinski, Z. Was (2010), 1011.0937
[10] LHC Higgs cross section working group, S. Dittmaier, C. Mariotti, G. Passarino, R. Tanaka (Eds.), *Handbook of LHC Higgs cross sections: 1. Inclusive observables* (2011), CERN-2011-002, 1101.0593
[11] LHC Higgs cross section working group, S. Dittmaier, C. Mariotti, G. Passarino, R. Tanaka (Eds.), *Handbook of LHC Higgs Cross Sections: 2. Differential distributions* (2012), CERN-2012-002, 1201.3084
[12] A. Djouadi, J. Kalinowski, M. Spira, Comput. Phys. Commun. **108**, 56 (1998), hep-ph/9704448
[13] A. Bredenstein, A. Denner, S. Dittmaier, M.M. Weber, Phys. Rev. **D 74**, 013004 (2006), hep-ph/0604011
[14] A. Bredenstein, A. Denner, S. Dittmaier, M.M. Weber, JHEP **02**, 080 (2007), hep-ph/0611234
[15] T. Melia, P. Nason, R. Rontsch, G. Zanderighi, JHEP **1111**, 078 (2011), 1107.5051
[16] N. Kauer, G. Passarino, JHEP **1208**, 116 (2012), 1206.4803
[17] J.M. Campbell, R.K. Ellis, C. Williams, JHEP **07**, 018 (2011), 1105.0020
[18] T. Gleisberg et al., JHEP **02**, 007 (2009), 0811.4622
[19] S. Jadach, Z. Was, R. Decker, J.H. Kuhn, Comput. Phys. Commun. **76**, 361 (1993)
[20] P. Golonka et al., Comput. Phys. Commun. **174**, 818 (2006)
[21] M.L. Mangano et al., JHEP **07**, 001 (2003), hep-ph/0206293
[22] S. Frixione, P. Nason, B.R. Webber, JHEP **08**, 007 (2003), hep-ph/0305252
[23] M. Aliev et al., Comput. Phys. Commun. **182**, 1034 (2011), 1007.1327
[24] G. Corcella et al., JHEP **01**, 010 (2001)
[25] J.M. Butterworth, J.R. Forshaw, M.H. Seymour, Z. Phys. **C 72**, 637 (1996), hep-ph/9601371
[26] ATLAS Collaboration, Eur. Phys. J. **C 70**, 823 (2010), 1005.4568
[27] S. Agostinelli et al., Nucl. Instrum. Meth. **A 506**, 250 (2003)
[28] ATLAS Collaboration, Eur. Phys. J. **C72**, 1909 (2012), 1110.3174
[29] ATLAS Collaboration, ATLAS-CONF-2012-047 (2012)
[30] ATLAS Collaboration, JHEP **12**, 060 (2010), 1010.2130
[31] M. Cacciari, G.P. Salam, G. Soyez, JHEP **04**, 063 (2008)
[32] S. Bolognesi, *et al.*, Phys. Rev. **D86**, 21 (2012)